One-Step Electrochemical Dealloying of 3D Bi-continuous Micro-nano Porous Bismuth Electrodes and CO_2RR Performance

Wenqin Lai , Yating Liu , Mingming Zeng , Dongmei Han , Min Xiao , Shuanjin Wang , Shan Ren * , Yuezhong Meng *

Posted Date: 16 May 2023

doi: 10.20944/preprints202305.1116.v1

Keywords: Nanoporous; Dealloying; 3D Architectures; CO2 reduction; formate

Article

One-Step Electrochemical Dealloying of 3D Bi-Continuous Micro-Nano Porous Bismuth Electrodes and CO_2RR performance

Wenqin Lai [1], Yating Liu [1], Mingming Zeng [1], Dongmei Han [1,2], Min Xiao [1], Shuanjin Wang [1], Shan Ren [1,*] and Yuezhong Meng [1,*]

[1] The Key Laboratory of Low-Carbon Chemistry & Energy Conservation of Guangdong Province, State Key Laboratory of Optoelectronic Materials and Technologies, School of Materials Science and Engineering, Sun Yat-sen University, Guangzhou 510275, P. R. China

[2] School of Chemical Engineering and Technology, Sun Yat-sen University, Zhuhai 519000, China;

* Correspondence: stsrs@mail.sysu.edu.cn（S.R.）, mengyzh@mail.sysu.edu.cn（Y.M.）

Abstract: The rapid development of electrochemical CO_2 reduction offers a promising route to convert intermittent renewable energy into products of high value-added fuels or chemical feedstocks. However, low faradaic efficiency, low current density, and a narrow potential range still limited the large-scale application of CO_2RR electrocatalyst. Herein, monolith 3D bi-continuous nano-porous Bismuth (np-Bi) electrodes are fabricated via a simple one-step electrochemical dealloying strategy from Pb-Bi binary alloy. The unique bi-continuous porous structure ensures highly effective charge transfer, meanwhile the controllable millimeter-size geometric porous structure enables easy catalyst adjustment to expose highly suitable surface curvatures with abundant reactive sites. This results in a high selectivity of 92.6% and superior potential window (400 mV, selectivity >88%) for electrochemical reduction of carbon dioxide to formate. Our scalable strategy provides a feasible pathway for mass-producing high-performance and versatile CO_2 electrocatalysts.

Keywords: nanoporous; dealloying; 3D Architectures; CO_2 reduction; formate

1. Introduction

The electrochemical reduction reaction of CO_2 (CO_2RR) is considered a promising method for producing useful carbon-containing compounds. [1–3] Formate or formic acid is one of the highly economically valuable fuel products of CO_2 electrocatalytic reduction. [4] Bismuth (Bi) has drawn particular attention for its ability to selectively convert CO2 into formic acid due to its low toxicity, low cost, and good stability, as well as low HER affinity and its strong binding to *OCHO species compared to other metal-based catalysts (Sn, Pb, Pd et-al.). [5–7] However, Bi-based electrocatalysts are still need to overcome the two-electron energy barriers for the activation of CO_2 to enhance the selectivity, current density and expend the high efficiency potential range. [8–10] To address these issues, a variety of nano Bismuth electrocatalysts including Bi nanoparticles (spherical or other shape) [11,12], Bi single atom [13], Bi nanosheets [14–16], Bi nanotubes [17], Bi nano-dendrite [18], have been rationally designed. Multitudinous nanostructure building strategies are introduced such as refining nanocrystal size, tailoring crystal facets, and surface functionalization with molecular coatings on contact region. [19,20] However, the construction of 3D nanostructures is still under limited study. Previous works are generally concentrated on combing nano-sized bismuth with 3D supporting substrates to enlarge the active surface area[21–23], which increases current density but often fails to reach high Faradaic Efficiency and a wide potential range. Therefore, it is still an urgent demand to create new types of 3D Bismuth nanostructures with tunable fine structure at a nanoscale level.

Dealloying is an efficient top-down method for producing 3D porous metals with a bi-continuous ligament-pore structure by selectively etching one or more active metal elements from alloys[24–26]. These monolithic bodies of nanoporous metals are widely used in the fields of Actuation, Sensing, and Energy Storage due to their large interfacial areas, tunable structure sizes,

 doi:10.20944/preprints202305.1116.v1

and good mechanical properties.[27] However, despite the self-freestanding inter-connected ligament nanostructures being rich in high-density under-coordinated active sites and possessing 3D hierarchical pore structures that facilitate interfacial mass transfer, their potential for catalytic applications remains largely unexplored. These materials have significant potential for industrial production.[28,29]

In this work, a scalable one-step electrochemical synthesis approach to fabricate a self-organized bi-continuous micro-nano porous bismuth electrode is reported. Our method utilizes electrochemical dealloying techniques to create a characteristic 3D bi-continuous nanoporous pure catalysis network with controllable geometric structures. The three-electrode H type cell electrocatalytic CO_2RR tests of np-Bi showcase the exceptional electrochemical performance, including high faradaic efficiency (92.6%) and superior potential window (~400 mV, selectivity >88%), for the reduction of carbon dioxide to formate. In addition, np-Bi catalyst also exhibits long-term stability for up to 12 hours.

2. Materials and Methods

2.1. Preparation of np-Bi electrode

Ingots of single-phase $Pb_{85}Bi_{15}$, $Pb_{88}Bi_{12}$, $Pb_{92}Bi_{8}$, $Pb_{98}Bi_{2}$ parent alloy were prepared separately by mixing Pb and Bi powder (99.999% purity, Shanghai Aladdin Bio-Chem Technology Co. Ltd) with an atomic ratio under argon atmosphere in a resistor furnace at 450 °C. The ingot was vacuum-sealed into a quartz glass tube and then repeated melting/solidification more than three times follow by quenching in water to maintain its geometric composition uniformity. Subsequently, it was cold-rolled to an alloy foil, annealed for 24 h at 130 °C under Argon atmosphere in a tube resistor furnace, precisely cut into 5*5*0.4 mm^3 cuboids. Electrodes were fabricated by attach an as-prepared alloy foil to a copper plate which was subsequently sealed in epoxy, only exposing one face of the alloy cuboids and the surface area is 0.25 cm^2.

Electrochemical dealloying was performed at a constant electro potential (-0.55V vs. MSE) for different selective times with Pt counter electrode and Hg/Hg_2SO_4 (MSE) reference electrode in 0.5 M HNO_3 aqueous electrolyte. The cell was settled in a circulating bath with a flow of heating/cooling water to making temperature control of 10, 25 or 45 ℃ during electrochemical processes. Afterwards, the as-dealloyed np-Bi sample was immersed in ultrapure deionized water for at least half hour and wash several times before further electrochemical measurement.

2.2. Electrochemical measurements

All the electrocatalytic CO_2RR tests were performed on a three-electrode H type cell using CHI-660e (CH Instruments, Shanghai, China) workstation. The Liner sweep voltammetry (LSV) measurements were conducted in 0.1 M $KHCO_3$ electrolyte saturated with N_2 or CO_2. The voltage ranges from -0.8 to -2.0 V (vs. SCE) and the scan rate was 50 mV s^{-1}. The electrochemical surface area (ECSA) of different electrodes was calculated from the Cyclic voltammetry (CV) experiments. CV test were performed within a none Faradaic processes potential range (-1.0 V to -0.8 V vs. SCE), in N_2 saturated 0.1 M $KHCO_3$ electrolyte. The scan rates were set to 10, 25, 50, 75, 100, 125, 150, 175 and 200 mV s^{-1}, respectively. Double-layer capacitance (C_{dl}) of the working electrodes were estimated by plotting the capacitive current density at -0.97 V (vs. SCE) against the scan rates. The measured slope of the linear regression differences between the electrodes referred to the net C_{dl} of catalysis. The ECSA value was in direct proportion to the ratio of C_{dl}. The Electrochemical impedance spectroscopies (EIS) measurements were carried out in N_2 saturated 0.1 M $KHCO_3$ electrolyte with 5 mV amplitude in a frequency range from 100 kHz to 0.1 Hz.

All the applied potentials were calibrated as reversible hydrogen electrode (RHE) potentials by using the Nernst equation as below.

$$E\ (\text{vs. RHE}) = E\ (\text{vs. SCE}) + 0.2412\text{V} + 0.0591 \times \text{pH} \quad (1)$$

Electrocatalytic CO_2RR tests were conducted in a homemade H-type electrolysis cell separated by a Nafion 117 membrane. Each compartment of the sealed cell contains 30 mL of 0.1 M $KHCO_3$

 doi:10.20944/preprints202305.1116.v1

electrolyte. The as-prepared np-Bi was directly used as the working electrode with $Hg/HgCl_2$ (saturated KCl) electrode placed in cathode chamber and Pt electrode was put in anode chamber. High-purity CO_2 gas was purged into the electrolyte in each compartment at a flow rate of 40ml min^{-1} for more than 30 min before electrocatalytic experiment. The pH values of electrolyte were measured to be ~6.8 after saturated by CO_2. Each chamber was kept stirring at 1000 r min^{-1} during electrolysis. The applied potential of the catalytic process was set on -1.5 V, -1.6 V, -1.7 V, -1.8 V, -1.9 V (vs. SCE) respectively. The catalytic time was 1h and the liquid phase products of the cathode cell were collected for quantitative analysis using a ^1H NMR (Bruker Avance III, 500MHz) after the electrocatalysis.

Typically, 500 μL of catholyte was uniformly mixed with 100 μL of deuterated water (D_2O) and 200 μL of internal standard of anhydrous dimethyl sulfoxide (DMSO, 99.9%). A water pre-saturation method was applied to the ^1H spectrum and the formate calibration curve was determined by internal standard (vs. 5 mM/L DMSO) method of using various concentrations (0.1, 0.5, 1.0, 2.0, 5.0 and 10 mM) of sodium formate (HCOONa). The Faradaic efficiency (FE) of specific productswas calculated via the following equation:

$$FE_{HCOOH} = \frac{nzF}{\mathrm{Q}} \times 100\% \quad (2)$$

Where F is Faraday constant and Z indicates the number of electron transfer. The amount of charge Q is the total electricity consumed during the electrolysis process.

3. Results and discussion

3.1. Fabrication and characterizations of nano-porous Bismuth (np-Bi) electrodes

In our previous study, it has been discovered that nanoporous Bi (np-Bi) can be converted into a Bi nanowire structure in a specific alloy composition through a designed electrochemical dealloying.[30] This suggested that modifications of the millimeter-size geometric porous structure from micrometer to nanometer scale can be achieved by simple changing of alloy composition. While the np-Bi nanowire matrix structure is too fragile to meet our goal to create a free-standing 3D pure catalysis electrode due to its low bismuth content (obtained through dealloying from $Sn_{99}Bi_1$ parent alloy), a Sn-Bi alloys with higher Bi content could causes the ligament size to split into two distinct scales, resulting in insufficiently small nanopores and disintegrated structures that cannot maintain the high activity required for the two-electron process of carbon dioxide reduction. Therefore, a suitable parent alloy and a designed alloy composition is essential to create a stable and active catalyst with the desired nanoporous structure.

In this study, four different solid solution contents of Pb-Bi alloy were selected to investigate the effect of component ranges on the nanostructure. Using the LSV curves (Figure S1, Supplementary Materials) of the parent alloy as guidance, the dissolution potential of the pure Bismuth in 0.5 M HNO_3 aqueous solution is more positive than the Pb-Bi parent alloy (>500mV), suggesting the bismuth is more stable than the lead at electrochemical environment. The constant dealloying potential is set at -0.55V vs. MSE in which the current density reaches 1 mA cm^{-2}. The XRD patterns of the as-prepared Pb-Bi parent alloy sample (Figure 1a) display a typical single Pb solid solution phase consistent with the phase diagram. Specifically, the three major peaks at 31.305°, 36.27°, and 52.23° are index to the (111), (200), and (220) patterns of cubic Pb (JCPDS, 04-0686), respectively. Other peaks are also well confine with the showed card and there is no Pb or Bismuth oxides peaks were observed. The crystal phase of the fully-dealloyed np-Bi is confirmed (Figure 1d), which show completely different patterns with three main peaks at 27.2°, 38.0°, and 39.6° that matches well with (012), (104), and (110) faces of rhombohedral Bi (JCPDS,44-1246). The narrow peaks exhibit the high crystalline structures and single phase of np-Bi. Energy-dispersive X-Ray spectroscopy (EDX) of as-dealloyed np-Bi (Figure S2, Supplementary Materials) shows none Pb element leaved in the porous structure, further confirms the high purity of the synthesized np-Bi catalyst. High magnification top-view SEM images (Figure 1b) reveal an open interpenetrating ligament-pore structure of $np\text{-}Bi_{12}$, with a uniform pore size of 280 nm and average ligament size of 290 nm.

Preprints (www.preprints.org) | NOT PEER-REVIEWED | Posted: 16 May 2023 doi:10.20944/preprints202305.1116.v1

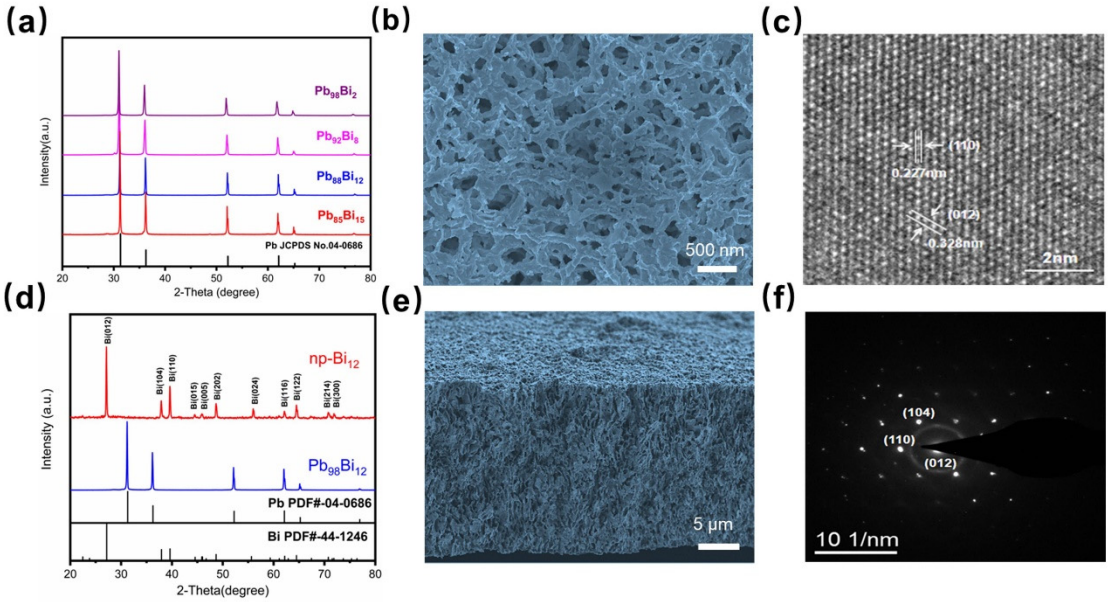

Figure 1. (a, d)) XRD patterns of as-prepared Pb-Bi parent alloys and np-Bi_{12} electrodes before and after dealloying; (b, e) SEM images of top-view and the cross-section of as-prepared np-Bi_{12} electrodes; (c, f) high-resolution transmission electron microscopy (HRTEM) images and selected area electron diffraction (SEAD) pattern of np-Bi_{12}.

The HRTEM image (Figure 1c) reveal well-resolved 2D lattice fringes with d spacings of 0.227 and 0.328 nm, which are coincided with the (110) and (012) lattice planes in the rhombohedral Bi structure. The SAED pattern further verifies the single-crystalline nature of np-Bi. (Figure 1f) The cross-sectional SEM images (Figure 1e) reveal a distinct growth pattern of the nanoporous structure differed from the top-view images. The top-view images show a uniformly distributed two-dimensional diffusion-like pattern of ligament framework, while the cross-sectional images demonstrate a longitudinal, interwoven nanowire structure growing downwards from the dealloying surface. (Figure S3, Supplementary Materials) This growth behavior deviates from traditional dealloying methods, which typically result in a uniform front-cross section. [31,32]Suggesting this electrochemical dealloying generates a unique morphology of the nanoporous structure with a preferred growth orientation in three dimensions. (Figure 2). During the dealloying process, Pb atoms were selectively dissolved layer by layer from the solid-liquid interface. Meanwhile, the remaining Bi atoms first underwent diffusion and agglomeration, followed by recrystallization. Finally, it stretched in three dimensions, ultimately formed a nanoporous structure. This phenomenon can be attributed to the high diffusion rate of bismuth atoms on the dealloying surface, which enables their long-range diffusion even in low bismuth content solid-solution alloys. The close atomic number proximity of lead and bismuth ensures their similar diffusivity during the dealloying and reorganization process, results in a closely-knit structure from the np-Bi ligaments to the pore channels, and the monolith nanostructure is reserve.[33]

Preprints (www.preprints.org) | NOT PEER-REVIEWED | Posted: 16 May 2023 doi:10.20944/preprints202305.1116.v1

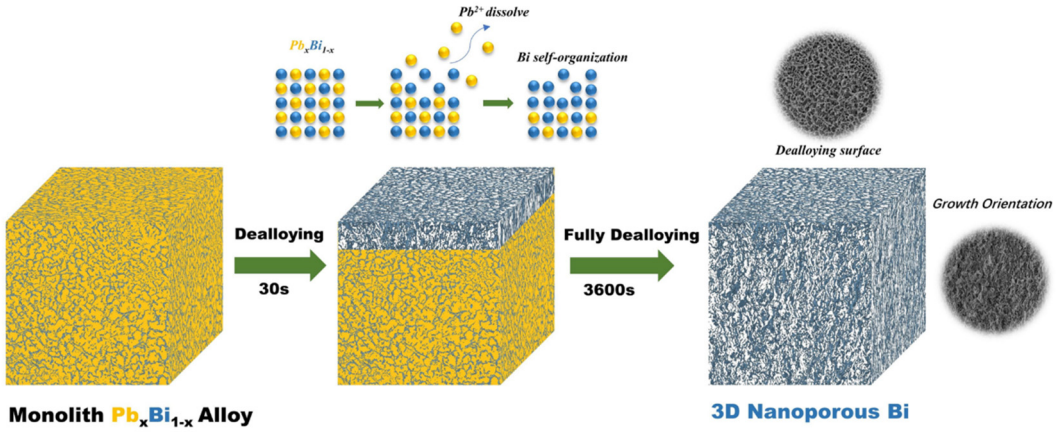

Figure 2. Schematic illustration of the dealloying and geometric growth of 3D nanoporous Bismuth.

The surface diffusion ability of stable component atoms at the dealloying interface is directly affected by the dealloying temperature, resulting in a change in the nanometer size. The effect of dealloying temperature (10°C, 45°C, 80°C) were investigated on dealloying of $Pb_{98}Bi_2$ alloy. (Figure S4, Supplementary Materials) At a dealloying temperature of 10°C, a sparse hierarchical three-dimensional porous foam structure is formed with a wide pore size distribution, including some large pores measuring 1.2 μm, as well as numerous small pores between 300-600 nm. Additionally, a root-like nanowire structure appears on the ligament with a diameter of about 30 nm. When dealloying temperature increase to 45°C, the resulting structure is still a hierarchical three-dimensional porous foam but shows greater differentiation of the hierarchical structure. Macropores rapidly grow with a distribution range of 2-10 μm, and the average macropore size increases to 5.59 μm, leading to an increase in pore size with an average size of 830 nm. Additionally, the ligament size grows to 760 nm, reflecting approximately a six-fold increase compared to the previous value of 130 nm at 10°C.At 80°C, the dealloying process results in a porous structure similar to nickel foam, lacking differentiation in structure. Fine nanowire branches and granular convex structures are absent, and pore walls change smoothly. Pore sizes range from 2-25 μm, with no pores smaller than 1 μm observed. The maximum observable pore size is 27.34 μm, the average pore size is 8.62 μm, with an average pore wall thickness of 4.84 μm. This demonstrate that the size of nanoporous structures increased continually with rising temperature, enabling control of nanoporous structure size across a wide range, from nanometers to micrometers, through adjustment of the dealloying temperature.

SEM images were used to investigate the changes in pore/ligament sizes and structural transformations of np-Bi of four selected Bismuth content after dealloying at 10℃, also revealing rapid shifts in the millimeter-size geometric porous structure of nanoporous Bismuth. The low magnification SEM image (Figure 3a-d) shows that, as the composition of the master alloy increases from 2 to 15 atom%, the average pore diameter gradually decreases, while the pore structure becomes more intact. The np-Bi_2 sample (Figure 3a) exhibits a few cracks, indicating that it undergoes large structural shrinkage and becomes very fragile when the alloy content is too low. On the other hand, the high magnification SEM image (Figure 3e-h) clearly reveals various pore structures for the with four components. The above Figure shows that all four alloy samples with different components exhibit a typical bi-continuous nanoporous structure with relatively rough surface pore walls under the same reaction conditions. As the bismuth content increases, the pore wall structure becomes more connected to form a cohesive whole, while decreasing the master alloy composition results in a decrease in connectivity and a change in porous structure morphology (Figure 3e). the np-Bi_2 porous structure has the weakest connectivity and appears empty and foamy, exhibiting a root-like nanowire morphology with a width of approximately 30nm and a length of 500 nm (Figure S5, Supplementary Materials).

Preprints (www.preprints.org) | NOT PEER-REVIEWED | Posted: 16 May 2023 doi:10.20944/preprints202305.1116.v1

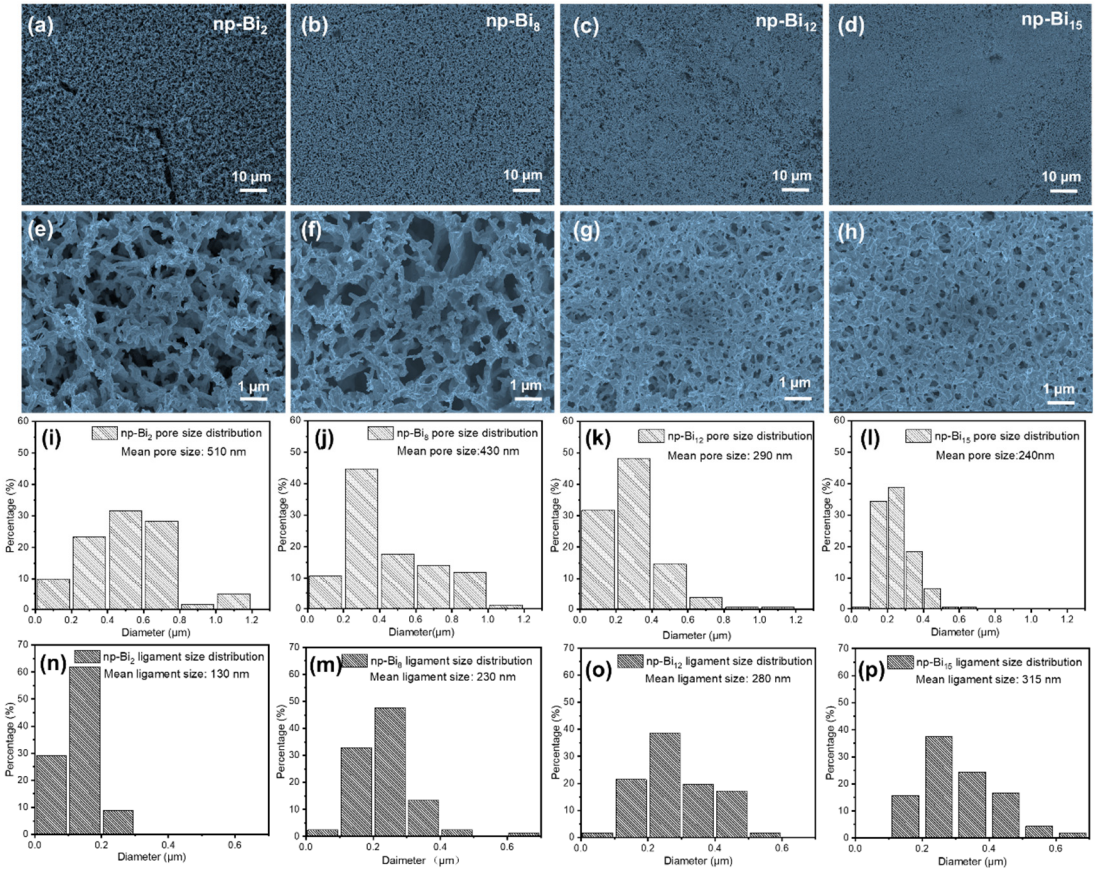

Figure 3. Top-view SEM images of alloy $Pb_{98}Bi_2$(a,c), $Pb_{88}Bi_{12}$(b, f),$Pb_{92}Bi_8$(c, g),$Pb_{85}Bi_{15}$ (d, h) after the potentiostatic dealloying , and its corresponding pore/ligament size distribution map (i-l,n-p). Applied potential is -0.55 V vs. MSE. Electrolyte is 0.5 M HNO_3 aqueous solution, dealloying temperature is 10℃.

Nano Measure software was used to measure the pore/ligament size of the sample and its distribution. It can be found that the maximum pore size of almost all components of the sample is less than 1200 nm. It is worth noting that several cases of pore size greater than 1200 nm can be observed in the np-Bi_8 sample. The open-door convey structure of np-Bi_8 has a similar foamy structure to np-Bi_2, with an average pore size of 430 nm and a ligament size of 230 nm, while the pore size distribution tends to be more uniform. Notably, the np-Bi_2 sample (Figure 3i, n) exhibits a hierarchical pore structure with an average pore size of 510 nm and a very small ligament size of 130 nm. As the Bi atomic content increases to 12 at%, the pore size gradually decreases to a minimum of 290 nm (Figure 3k, o), while ligament size increases from 130 nm to 280 nm, and the differences in pore and ligament sizes become less pronounced. However, the np-Bi_{15} sample has the narrowest pore size distribution of 240 nm, but the distribution of ligament sizes is wider with a mean size of 315 nm. (Figure 3i, p) This indicates an inflection point in the geometric porous structure at the bismuth atomic ratiol of 12%, where the channels and pore walls are most uniform and interconnected with sufficient surface roughness, while still maintaining a few large channels (800-1000 nm). (Figure S6, Supplementary Materials) This unique structure had the potential to expose a large number of edge atoms and facilitate quick mass transfer while maintaining excellent structural integrity.

3.2. The CO_2RR activity of np-Bi samples with different morphology

The CO_2RR performances of the prepared nanoporous electrodes were systematically evaluated in CO_2-saturated 0.1 M $KHCO_3$ electrolyte using a H-type cell. LSV analysis was conducted to investigate the influence of different morphologies on the competing hydrogen evolution reaction (HER) (Figure 4a). The onset potentials and cathodic currents for all four samples in CO_2-saturated electrolyte is significantly positive than those observed in N_2-saturated electrolyte. Specifically, the

 doi:10.20944/preprints202305.1116.v1

onset potential of np-Bi in CO_2-saturated electrolyte is 350 mV more positive than that of samples in N_2 atmosphere, this resulted in a dramatic increase in current density of np-Bi at the same potential. Suggesting that np-Bi are more favors the catalysis of CO_2RR rather than hydrogen evolution reaction (HER). Furthermore, the more uniform np-Bi_{12} and np-Bi_{15} electrodes exhibit higher onset potentials and current densities than np-Bi_2 and np-Bi_8 electrodes, Among the four samples, np-Bi_{12} show the highest current density for CO_2RR, at 26.2 mA cm^{-2} with -1.2 V vs. RHE compared to np-Bi_2 (19.3mA cm^{-2}), np-Bi_8 (20.8 mA cm^{-2}), and np-Bi_{15} (23.2 mA cm^{-2}), indicating that structural uniformity can reveal numerous active sites with high intrinsic catalytic activity. Electrochemically active surface area (ECSA) of four different morphologies np-Bi were compared by analyzing their double-layer capacitances (C_{dl}) obtained from cyclic voltammetry (CV) tests to confirm their electrocatalytic activities (Figure S7, Supplementary Materials). The ECSA generally increase with increasing Bi content, with np-Bi_{12} exhibiting the highest calculated C_{dl} value of 13.01 mF cm^{-2}. This is almost 9-fold increase from the hierarchically structured np-Bi_2 to the uniform np-Bi_{12}. The np-Bi_{15} sample showed a slightly deteriorate C_{dl} value of 12.44 mF cm^{-2} may due to variations in ligament size distribution (Figure 4b). The results suggest that the uniform shape of nanopores and connection ligaments in np-Bi_{12} not only produces heightened roughness on its edge sites, but facilitating the penetration of the electrolyte, increasing the contact area between the catalyst and electrolyte. This enhances the accessibility of active sites for CO_2 adsorption, activation, and reduction. Moreover, as displayed in the Nyquist plots (Figure 4c) measured by electrochemical impedance spectroscopy (EIS) analysis, charge transfer resistance of the four electrodes varies with increasing Bi content, the Nyquist plots of np-Bi_8 and np-Bi_2 electrodes show a large arcs sizes compared with np-Bi_{12} and np-Bi_{15} electrodes. The most uniform np-Bi_{12} electrodes exbibit the lowest arcs size of all sample, indicating that high-efficiency charge transfer phenomenon happened in the CO_2RR process. These outcomes highlight the importance of preserving the integral uniform structure of np-Bi_{12} in maximizing catalytic activity.

Electrolysis tests were conducted to evaluate the different morphologies of np-Bi samples as a catalyst for formic acid generation and uncovering the structure-performance correlations. As show in Figure 4d, the formate Faraday efficiency (FE) of four np-Bi electrodes all demonstrate an initial increase followed by a decline at higher potentials, with all catalysts reaching their maximum efficiency at -0.956V. The np-Bi_{12} sample display the highest selectivity for $HCOO^-$, with a Faraday efficiency of 92.16%, while the np-Bi_{15} sample only achieve a seletivity of 88.8%. In contrast, the np-Bi_8 and np-Bi_2 samples exhibited lower efficiencies due to structural connectivity loss and larger pore size, resulting in maximum efficiencies of 74.5% and 76.7%, respectively (Table S1, Supplementary Materials). To demonstrate the superior activity of np-Bi, we conducted used bulk pure Bi plates of the same size as a blank control group. As shown in Figure 4e, pure Bi achieve only 40-60% Faraday efficiency over the entire potential range, with the highest FE reaching only 65%, which is much lower than the as-synthesized np-Bi_{12} electrodes. This suggests that the nanoporous np-Bi structure exhibits a higher intrinsic catalytic activity and provides abundant active sites, which facilitate CO_2 absorption and lower the *OCHO binding energy required for the generation of formic acid instead of hydrogen evolution reaction (HER). However, it's important to note that an inappropriate geometric nanoporous structure like np-Bi_2 may not make full use of these active sites. Interestingly, np-Bi_{12} electrode maintained a consistently high Faraday efficiency (>88%) form -0.85V to -1.25V, showing a wide, highly efficiency potential window of 400 mV. In contrast, high selectivity for $HCOO^-$ (>80%) in np-Bi_{15} electrode is only achieved within a narrow potential range of ~100mV. This phenomenon may attribute to the highly uniform bi-continuous ligament/pore structures. The unique roughness and highly curved surface of the np-Bi_{12} can ascend the concentrate of CO_2 near the active sites and stronger the adsorption of the CO_2 intermediates. [17,34]

Preprints (www.preprints.org) | NOT PEER-REVIEWED | Posted: 16 May 2023 doi:10.20944/preprints202305.1116.v1

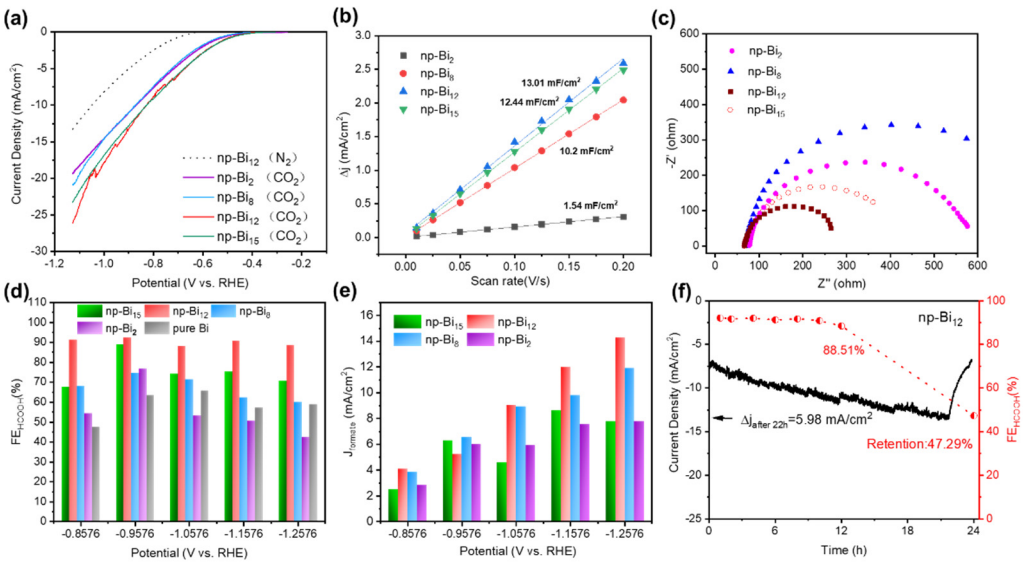

Figure 4. (a) The LSV curve of np-Bi electrodes under N_2 or CO_2 gas saturation. (b) Linear fitting ECSA value of four different nanoporous Bi electrodes, (c) Nyquist plots for nanoporous Bi with four different morphologies. (d) The performance of the electrocatalytic reduction of carbon dioxide by four nanoporous Bi samples with different morphologies. (e) the partial current densities of formic acid. (f) long-term stability test of np-Bi_{12}.

Figure S8(Supplementary Materials) shows that the total current density of np-Bi electrodes increases as the applied potential becomes more negative. Even with an applied potential shift of -1.256 V vs RHE compared to np-Bi electrodes, the current density of pure Bi never surpasses 9 mA cm^{-2} in the hole potential range. This phenomenon suggests that the unique nanoporous structures plays play a crucial role in enhancing the electrocatalytic performance. The np-Bi_2 and np-Bi_8 samples exhibit high total current densities above 13 mA cm^{-2} at -1.156 V and -1.256 V, with a maximum value of 18.3 and 19.8 mA cm^{-2}, while the total current density of np-Bi_{12} and np-Bi_{15} only achieve the highest of 16.1 and 10.7 mA cm^{-2}. Cross-references form the Figure 4e, Faraday efficiency of np-Bi_2 and np-Bi_8 for formic acid is very low, resulting in a large amount of catalysis current has been distributed to generate other products. This implies that the nanoporous structures of np-Bi_2 and np-Bi_8 electrodes also have a certain catalysis activity on the contact suface, but suffer from competitive reactivity of HER at high potentials, which hinders and reduces the selectivity of formic acid. The partial current densities of formic acid of four np-Bi electrodes are summarized in Figure 4e, shows agreement with our theory, with np-Bi_{12} achieving the highest partial current density (14.2 mA cm^{-2}) at -1.25 V compared to other np-Bi electrodes.

A constant electrolysis test was conducted at -0.965 V vs RHE to assess the long-term performance (Figure 4f) and structural stability of np-Bi_{12} in CO_2 reduction reaction (CO_2RR). CO_2-saturated 0.1 M $KHCO_3$ aqueous solution was used as an electrolyte under a constant potential of -0.956 V vs RHE, during the entire 24 hours of the test. The np-Bi_{12} electrode display stable activity over the first 12 hours of the experiment, with minor fluctuations in Faradaic efficiency above 88.5%. The current density showed larger fluctuations due to the accumulation of gaseous products on the surface of electrodes caused by continuous purging of CO_2 in the cathodic compartment at a flow rate of 40 mL/min. After 24 hours of electrolysis, the Faraday efficiency of formate decrease to 47.29%. To investigate the possible changes in morphology and structure after the long-term stability test, SEM and EDS analyses were performed (Figure S9, Supplementary Materials). The SEM image display various small nanosheets covering the porous surface. The EDS pattern and atomic ratio calculations indicated that Bi_2O_3 nanosheets had grown on the nanoporous surface. However, the effects of these nanosheets differ from those produced in the reference study, where a Bi/Bi_2O_3 structure supported formate production. [35,36]. This demonstrates the excellent stability of np-Bi_{12} under continuous catalytic conditions over a 12-hour period.

4. Conclusions

In conclusion, a cost-effective and scalable one-step electrochemical dealloying method was successfully developed to fabricate monolith 3D bi-continuous nano-porous bismuth electrodes for efficient CO_2 reduction. Selective electrochemical dealloying etched and dissolved lead phase of the Pb-Bi parent alloy from the contact surface, the high diffusion rate of bismuth atoms leaded to the growth of 3D hierarchical nanoporous bismuth with a preferred growing orientation downwards from the dealloying surface. The geometric structure and pore size of the nanoporous bismuth electrode can be readily controlled by varying the dealloying parameters. The fine engineered inter-connected uniform ligament/pore nanoporous bismuth-based electrodes (np-Bi_{12}) receive abundant active sites, low charge transfer resistance and enhanced intrinsic activity compared with other np-Bi electrodes. Featured exceptional electrocatalytic properties with a high fomate FE of 92.6% at -0.956V vs. RHE, high current density of 14.2 mA cm^{-2} at -1.25V vs. RHE and a wide potential window of 400 mV for selective CO_2 electrochemical conversion. This innovative method of introducing monolith 3D bi-continuous micro-nanoporous Bismuth can lead to insights into the design of advanced 3D nanomaterials for sustainable energy technologies.

Supplementary Materials: The following supporting information can be downloaded at the website of this paper posted on Preprints.org, Figure S1: Linear sweep voltammetry curves of $Pb_{98}Bi_2$、$Pb_{92}Bi_8$、$Pb_{88}Bi_{12}$、$Pb_{85}Bi_{15}$ alloy; Figure S2: EDS analyses of $Pb_{98}Bi_{15}$ alloy before (a) and after dealloying (b) and (c)element qualitative analysis; Figure S3: cross-section SEM images of np-Bi_{12} sample; Figure S4: Top-view SEM images of $Pb_{98}Bi_2$ alloy after the potentiostatic dealloying at 10℃、45℃and 80℃; Figure S5: High-resolution scanning electron micrograph of np-Bi_2 sample; Figure S6: Distribution diagram of the average pore size and ligament size of nano-porous Bi samples as a function of composition; Figure S7: Cyclic voltammetry (CV) curves of np-Bi_2, np-Bi_8，np-Bi_{12}, np-Bi_{15} at different scanning speeds; Figure S8: Time-dependent current density curves of np-Bi_{12} at different potentials and the calculated total current density (J_{total}) values of four nanoporous electrodes; Figure S9: Low and high magnification SEM images of np-Bi_{12} electrodes after 24h of long-term electrolysis test; Table S1: The relationship between the size of four nanoporous Bi samples with different morphologies and the Faraday efficiency of formic acid.

Author Contributions: Conceptualization, W.L., S.R. and Y.M.; methodology, W.L.; software, W.L. and Y.L.; validation, W.L., and S.R.; formal analysis, W.L.; investigation, W.L.; resources, D.H., M.X., S.W. and Y.M.; data curation, W.L., Y.L. and M.Z.; writing—original draft preparation, W.L.; writing—review and editing, W.L., D.H., M.X., S.W., S.R. and Y.M.; visualization, W.L.; supervision, S.R. and Y.M.; project administration, S.R. and Y.M.; funding acquisition, S.R. and Y.M.

Funding: This research was funded by the Guangzhou Scientific and Technological Planning Project (Grant No.201707010424) and Major Special Projects in Guangdong Province (Grant No. 2016B010114004)

Data Availability Statement: Not applicable.

Conflicts of Interest: The authors declare no conflict of interest.

References

1. Solomon, S.; Plattner, G.-K.; Knutti, R.; Friedlingstein, P. Irreversible Climate Change Due to Carbon Dioxide Emissions. *Proceedings of the national academy of sciences* **2009**, *106*, 1704–1709.
2. De Luna, P.; Hahn, C.; Higgins, D.; Jaffer, S.A.; Jaramillo, T.F.; Sargent, E.H. What Would It Take for Renewably Powered Electrosynthesis to Displace Petrochemical Processes? *Science (1979)* **2019**, *364*, eaav3506.
3. Nitopi, S.; Bertheussen, E.; Scott, S.B.; Liu, X.; Engstfeld, A.K.; Horch, S.; Seger, B.; Stephens, I.E.L.; Chan, K.; Hahn, C. Progress and Perspectives of Electrochemical CO2 Reduction on Copper in Aqueous Electrolyte. *Chem Rev* **2019**, *119*, 7610–7672.
4. Grasemann, M.; Laurenczy, G. Formic Acid as a Hydrogen Source–Recent Developments and Future Trends. *Energy Environ Sci* **2012**, *5*, 8171–8181.
5. Han, N.; Ding, P.; He, L.; Li, Y.; Li, Y. Promises of Main Group Metal–Based Nanostructured Materials for Electrochemical CO2 Reduction to Formate. *Adv Energy Mater* **2020**, *10*, 1902338.
6. Kim, C.; Dionigi, F.; Beermann, V.; Wang, X.; Möller, T.; Strasser, P. Alloy Nanocatalysts for the Electrochemical Oxygen Reduction (ORR) and the Direct Electrochemical Carbon Dioxide Reduction Reaction (CO2RR). *Advanced Materials* **2019**, *31*, 1805617.

7. García de Arquer, F.P.; Bushuyev, O.S.; De Luna, P.; Dinh, C.; Seifitokaldani, A.; Saidaminov, M.I.; Tan, C.; Quan, L.N.; Proppe, A.; Kibria, M.G. 2D Metal Oxyhalide-derived Catalysts for Efficient CO2 Electroreduction. *Advanced Materials* **2018**, *30*, 1802858.
8. Gao, T.; Wen, X.; Xie, T.; Han, N.; Sun, K.; Han, L.; Wang, H.; Zhang, Y.; Kuang, Y.; Sun, X. Morphology Effects of Bismuth Catalysts on Electroreduction of Carbon Dioxide into Formate. *Electrochim Acta* **2019**, *305*, 388–393.
9. Zhang, X.; Hou, X.; Zhang, Q.; Cai, Y.; Liu, Y.; Qiao, J. Polyethylene Glycol Induced Reconstructing Bi Nanoparticle Size for Stabilized CO2 Electroreduction to Formate. *J Catal* **2018**, *365*, 63–70.
10. Yang, Z.; Oropeza, F.E.; Zhang, K.H.L. P-Block Metal-Based (Sn, In, Bi, Pb) Electrocatalysts for Selective Reduction of CO2 to Formate. *APL Mater* **2020**, *8*, 060901.
11. Wu, D.; Wang, X.; Fu, X.-Z.; Luo, J.-L. Ultrasmall Bi Nanoparticles Confined in Carbon Nanosheets as Highly Active and Durable Catalysts for CO2 Electroreduction. *Appl Catal B* **2021**, *284*, 119723.
12. Zhang, X.; Hou, X.; Zhang, Q.; Cai, Y.; Liu, Y.; Qiao, J. Polyethylene Glycol Induced Reconstructing Bi Nanoparticle Size for Stabilized CO2 Electroreduction to Formate. *J Catal* **2018**, *365*, 63–70.
13. Zhang, E.; Wang, T.; Yu, K.; Liu, J.; Chen, W.; Li, A.; Rong, H.; Lin, R.; Ji, S.; Zheng, X. Bismuth Single Atoms Resulting from Transformation of Metal–Organic Frameworks and Their Use as Electrocatalysts for CO2 Reduction. *J Am Chem Soc* **2019**, *141*, 16569–16573.
14. Yang, F.; Elnabawy, A.O.; Schimmenti, R.; Song, P.; Wang, J.; Peng, Z.; Yao, S.; Deng, R.; Song, S.; Lin, Y. Bismuthene for Highly Efficient Carbon Dioxide Electroreduction Reaction. *Nat Commun* **2020**, *11*, 1088.
15. Han, N.; Wang, Y.; Yang, H.; Deng, J.; Wu, J.; Li, Y.; Li, Y. Ultrathin Bismuth Nanosheets from in Situ Topotactic Transformation for Selective Electrocatalytic CO2 Reduction to Formate. *Nat Commun* **2018**, *9*, 1320.
16. Wu, D.; Huo, G.; Chen, W.; Fu, X.-Z.; Luo, J.-L. Boosting Formate Production at High Current Density from CO2 Electroreduction on Defect-Rich Hierarchical Mesoporous Bi/Bi2O3 Junction Nanosheets. *Appl Catal B* **2020**, *271*, 118957.
17. Fan, K.; Jia, Y.; Ji, Y.; Kuang, P.; Zhu, B.; Liu, X.; Yu, J. Curved Surface Boosts Electrochemical CO2 Reduction to Formate via Bismuth Nanotubes in a Wide Potential Window. *ACS Catal* **2019**, *10*, 358–364.
18. Tran-Phu, T.; Daiyan, R.; Fusco, Z.; Ma, Z.; Amal, R.; Tricoli, A. Nanostructured B-Bi2O3 Fractals on Carbon Fibers for Highly Selective CO2 Electroreduction to Formate. *Adv Funct Mater* **2020**, *30*, 1906478.
19. Lee, C.W.; Hong, J.S.; Yang, K.D.; Jin, K.; Lee, J.H.; Ahn, H.-Y.; Seo, H.; Sung, N.-E.; Nam, K.T. Selective Electrochemical Production of Formate from Carbon Dioxide with Bismuth-Based Catalysts in an Aqueous Electrolyte. *ACS Catal* **2018**, *8*, 931–937.
20. Tan, X.; Yu, C.; Ren, Y.; Cui, S.; Li, W.; Qiu, J. Recent Advances in Innovative Strategies for the CO 2 Electroreduction Reaction. *Energy Environ Sci* **2021**, *14*, 765–780.
21. Rabiee, H.; Ge, L.; Zhang, X.; Hu, S.; Li, M.; Smart, S.; Zhu, Z.; Yuan, Z. Shape-Tuned Electrodeposition of Bismuth-Based Nanosheets on Flow-through Hollow Fiber Gas Diffusion Electrode for High-Efficiency CO2 Reduction to Formate. *Appl Catal B* **2021**, *286*, 119945.
22. Ma, T.; Wu, Z.; Wu, H.; Cai, W.; Wen, Z.; Wang, L.; Jin, W.; Jia, B. Engineering Bi-Sn Interface in Bimetallic Aerogel with 3D Porous Structure for Highly Selective Electrocatalytic CO2 Reduction to HCOOH. *Angew. Chem. Int. Ed* **2021**, *60*, 12554–12559.
23. Jing, X.-T.; Zhu, Z.; Chen, L.-W.; Liu, D.; Huang, H.-Z.; Tian, W.-J.; Yin, A.-X. Boosting CO2 Electroreduction on Bismuth Nanoplates with a Three-Dimensional Nitrogen-Doped Graphene Aerogel Matrix. *ACS Appl Mater Interfaces* **2023**.
24. McCue, I.; Benn, E.; Gaskey, B.; Erlebacher, J. Dealloying and Dealloyed Materials. *Annu Rev Mater Res* **2016**, *46*, 263–286.
25. An, Y.; Tian, Y.; Wei, C.; Tao, Y.; Xi, B.; Xiong, S.; Feng, J.; Qian, Y. Dealloying: An Effective Method for Scalable Fabrication of 0D, 1D, 2D, 3D Materials and Its Application in Energy Storage. *Nano Today* **2021**, *37*, 101094.
26. Shi, H.; Tang, C.; Wang, Z.; Zhang, Z.; Liu, W.; Ding, Y.; Shen, X. Nanoporous Bismuth Electrocatalyst with High Performance for Glucose Oxidation Application. *Int J Hydrogen Energy* **2021**, *46*, 4055–4064.
27. Wu, X.; He, G.; Ding, Y. Dealloyed Nanoporous Materials for Rechargeable Post-Lithium Batteries. *ChemSusChem* **2020**, *13*, 3376–3390.
28. Liu, P.; Guan, P.; Hirata, A.; Zhang, L.; Chen, L.; Wen, Y.; Ding, Y.; Fujita, T.; Erlebacher, J.; Chen, M. Visualizing Under-coordinated Surface Atoms on 3D Nanoporous Gold Catalysts. *Advanced Materials* **2016**, *28*, 1753–1759.
29. Wang, X.; Luo, M.; Lan, J.; Peng, M.; Tan, Y. Nanoporous Intermetallic Pd3Bi for Efficient Electrochemical Nitrogen Reduction. *Advanced Materials* **2021**, *33*, 2007733.
30. Li, K.; Hong, L.; Han, D.; Wang, S.; Xiao, M.; Meng, Y.; Bao, D.; Ren, S. Fabrication of Porous Bismuth by Electrochemical Dealloying of Sn–Bi Alloys: From Microporous Structures to Nanowire Matrix Composites. *Electrochem commun* **2017**, *81*, 88–92.

31. Erlebacher, J.; Aziz, M.J.; Karma, A.; Dimitrov, N.; Sieradzki, K. Evolution of Nanoporosity in Dealloying. *Nature* **2001**, *410*, 450–453.
32. Zhang, W.; Xu, C.; Hu, Y.; Yang, S.; Ma, L.; Wang, L.; Zhao, P.; Wang, C.; Ma, J.; Jin, Z. Electronic and Geometric Structure Engineering of Bicontinuous Porous Ag–Cu Nanoarchitectures for Realizing Selectivity-Tunable Electrochemical CO2 Reduction. *Nano Energy* **2020**, *73*, 104796.
33. Seebauer, E.G.; Allen, C.E. Estimating Surface Diffusion Coefficients. *Prog Surf Sci* **1995**, *49*, 265–330.
34. Zhang, W.; Yang, S.; Jiang, M.; Hu, Y.; Hu, C.; Zhang, X.; Jin, Z. Nanocapillarity and Nanoconfinement Effects of Pipet-like Bismuth@ Carbon Nanotubes for Highly Efficient Electrocatalytic CO2 Reduction. *Nano Lett* **2021**, *21*, 2650–2657.
35. Dutta, A.; Zelocualtecatl Montiel, I.; Kiran, K.; Rieder, A.; Grozovski, V.; Gut, L.; Broekmann, P. A Tandem (Bi2O3→ Bimet) Catalyst for Highly Efficient Ec-CO2 Conversion into Formate: Operando Raman Spectroscopic Evidence for a Reaction Pathway Change. *ACS Catal* **2021**, *11*, 4988–5003.
36. Liu, S.; Lu, X.F.; Xiao, J.; Wang, X.; Lou, X.W. Bi2O3 Nanosheets Grown on Multi-channel Carbon Matrix to Catalyze Efficient CO2 Electroreduction to HCOOH. *Angewandte Chemie* **2019**, *131*, 13966–13971.